Indian J. Phys. **66B** (5 & 6), 651 – 672 (1992)

Numerical simulation of inertial confinement fusion targets

N K Gupta and S V Lawande
Theoretical Physics Division, Bhabha Atomic Research Centre,
Bombay-400 085, India

Abstract : The dynamics of an inertial confinement fusion (ICF) experiment involves a variety of complex phenomena such as driver (laser or ion) beam interaction with plasma, charged particle transport and collisional processes, nuclear fusion reaction kinetics, hydrodynamics and thermodynamics of the plasma etc. The simultaneous presence of these several processes necessitates the use of numerical methods to study ICF targets. Various laboratories in the world engaged in ICF research have evolved their own strategies for developing the computer simulation codes. Our efforts at BARC in this direction will be highlighted in this paper. The paper will essentially concentrate on three main features, namely the incident beam energy absorption, the hydrodynamics of the plasma, and an appropriate equation of state (EOS) model. Limitations of the often used Von-Neumann prescription of artificial viscous pressure for shocks will be discussed with the help of benchmark problems. Salient features of recently developed high resolution UPWIND Schemes will be highlighted. A semi-empirical EOS model used in our code will be described and compared with the best known results from SESAME, EOS Library of USA. Except near the region of phase transition, the adopted EOS model gives satisfactory results. Finally, some discussion and results are presented for the energy absorption profiles of laser and ion beam in ICF plasma.

Keywords : Numerical simulations, inertial confinement fusion, hydrodynamics, upwind schemes, equation of state.

PACS Nos. : 52.25.kn, 52.50.Lp, 52.65.+z

1. Introduction

A practical inertial confinement fusion (ICF) scheme is based on the implosion of small D-T pellets driven by either direct laser/ion beams [1] or a secondary driver such as X-rays generated by the incident laser/ion beam [2]. The outer surface of the pellet gets heated up, ionizes and ablates off to surround the pellet in a cloud of low density plasma which continue to absorb the incident energy. This energy continues to heat the pellet driving in turn the ablation processes. The high pressures produced thereby results in the generation of inward moving shock waves because of rocket action. By suitably tailoring the incident beam, it is possible to generate a sequence of non-overlapping shocks of increasing strength which coalesce near the centre of the pellet [3]. The so formed coalesced shock leads to further compression and heating while moving inwards till it is reflected at the centre. This reflected shock again enhances the compression and heating. Thus in a small region around the centre, the density and temperature become large enough to trigger the thermonuclear reactions. The

alpha particles released in these reactions also contribute to heating the central zone. Since the range of alpha particles increases with temperature, a burn wave propagates which rapidly engulfs the entire pellet. This causes a significant (~30%) fraction of the fuel to be burnt up before the pellet disintegrates.

The dynamics of such an ICF scheme involves a variety of complex phenomena such as driver beam plasma interactions, charge particle transport and collisional processes, nuclear fusion reaction kinetics, hydrodynamic and thermodynamic behaviour of the plasma etc. Although the essential physics involved in any single process can usually be described by simple analytical models, simultaneous presence of several processes occurring in ICF requires the complete dynamics of the pellet implosion be simulated using a computer code that contains all the relevant information. Various laboratories in the world engaged in ICF research have evolved their own strategies for developing the computer simulation codes [4–8]. A versatile two dimensional code such as LASNEX [6] developed at Lawrence Livermore Laboratory has three hydrodynamic equations separately for electrons and ions and they are coupled to the Maxwell's equations through electric and magnetic fields. These sets of equations are solved numerically in a consistent manner. On the other hand, some simpler codes [5, 7–8] treat the plasma as quasi-neutral (no charge separation) and thus ignore the generation of electric and magnetic fields. These codes essentially describe the ICF plasma through one fluid, two temperature hydrodynamic equations. However, all ICF codes must have a fairly accurate prescription for the three processes, namely the incident beam absorption, the hydrodynamics of the plasma and the appropriate equation of state (EOS). In this paper, we will be essentially concentrating on these three aspects of ICF target simulations.

2. Hydrodynamics of the target

2.1. Basic equations :

The basic starting point for any ICF target simulation code are hydrodynamic equations describing the conservation of mass, momentum and energy. In Lagrangean geometry they can be written as

Energy conservation :

$$\left(\frac{\partial U}{\partial T}\right)_\rho \frac{\partial T}{\partial t} + \left(\frac{\partial U}{\partial \rho}\right)_T \frac{\partial \rho}{\partial t} + p\frac{\partial V}{\partial t} = S. \tag{1}$$

Momentum conservation :

$$\frac{\partial u}{\partial t} = -\frac{1}{\rho}\nabla p \equiv r^\alpha \frac{\partial p}{\partial m}. \tag{2}$$

Mass conservation :

$$\frac{\partial r}{\partial t} = u(r,t). \tag{3}$$

In these equations the symbols U, T, ρ, p and S respectively denote the total internal energy, temperature, density, total pressure and total energy source. The particle velocity $u(r, t)$ is

related to the Lagrangean coordinate r through the mass conservation equation (3). The mass coordinate m is related to the volume coordinate v as

$$dm = \frac{1}{\vartheta} d\vartheta \tag{4}$$

where the volume element dv is defined as

$$d\vartheta = \frac{1}{\alpha + 1} d\left(r^{\alpha+1}\right). \tag{5}$$

The geometry factor α takes the values of 0, 1 and 2 for plane, cylindrical and spherical geometries. These equations are completed through the equation of state which relates the pressure and internal energy to the density and temperature. Formally, we have written down these equations for one fluid. In principle, the energy equation is split into two, one for electron and the other for ion. If one considers the plasma to be quasi-neutral, one has only one momentum balance equation as electrons and ions are assumed to move with same common velocity to avoid charge separation. Mass of the electrons is usually neglected. The energy source term S in equation (1) contains all the sources; internal as well as external. For a typical hydrodynamic simulation of ICF plasma, the source term can be formally written as

$$S = H + Y - J + X \tag{6}$$

where H represents the flow of heat due to thermal conduction, Y is the rate of thermonuclear energy release, J is the rate of radiation loss from the plasma and X denotes the rate of external energy source (*e.g.* laser or ion beam energy deposited to the plasma). The commonly used form for these terms are described below.

The heat conduction term is calculated as

$$H \doteq \frac{1}{\rho} \nabla . K \nabla T \tag{7}$$

where ρ is the plasma density. The thermal conductivity coefficient K is written as for one temperature model

$$K = K_i + K_e . \tag{8}$$

The ion contribution K_i is given as

$$K_i = 4.55 \times 10^{-11} T^{5/2} (\log \Lambda)^{-1} \left[\bar{A}\bar{Z}^{-2}\right]^{1/2} \bar{Z}^2 \varepsilon\delta \tag{9}$$

with

$$\varepsilon\vartheta = \frac{0.43\bar{Z}}{(3.44 + \bar{Z} + 0.26 \log \bar{Z})} \tag{10}$$

The coloumb logarithm Λ is given by

$$\Lambda = 1.24 \times 10^6 T^{3/2} ne^{-1/2} \Big/ \bar{Z} \tag{11}$$

In these expressions, $\bar{Z}$ denotes the average ion charge. $\bar{A}$ is the average atomic number of the plasma and ne denotes the electron number density. The electron thermal conductivity coefficient K_e is free streaming limited and is written as

$$K_e = K_e' \left[1 + \left(\frac{a\lambda_e}{T} \right) \frac{dT}{dr} \right]^{-1} \tag{12}$$

where λ_e is the electron mean free path

$$\lambda_e = 5.7 \times 10^7 \, T^2 / n_i \bar{Z}^2 \tag{13}$$

and 'a' is the free streaming constant. The empirical constant 'a' is obtained through a series of experiments and may depend upon the problem under study. A value of 0.03 can be used for typical ICF simulations. The electron thermal conductivity coefficient K_e is given as

$$K_e' = 1.955 \times 10^{-9} T^{5/2} (\log \Lambda)^{-1} \bar{Z} \, \varepsilon\delta / \bar{Z}^2. \tag{14}$$

The radiation loss from the plasma is dominated by Bremsstrahlung radiation emitted by the electron and the term J in eq. (6) can be written as

$$J = 8.5 \times 10^{-14} n_e \sqrt{T} \, \bar{Z}^2 / \bar{A} \tag{15}$$

All these expressions for the energy source terms are in the units of Watts/kg. The incident beam energy deposition term X will be described in Section 4.

The sudden deposition of beam energy leads to the generation of shock waves and in turn rarefaction waves and contact discontinuities. As is well known, a shock wave moves as a discontinuity in state variables [9]. A discontinuity in state variables (density, pressure, particle velocity etc.) requires special attention in numerical calculations. The classical method, proposed by von-Neumann and Richtmyer [10], consists of introducing a purely artificial dissipative mechanism of such a form and strength that the discontinuity in state variables is replaced by a smooth transition extending over a small number (say three or four) of space intervals. For one dimensional problem they proposed an artificial viscous pressure q to be added to the physical pressure term, of the form

$$q = \begin{cases} b. \, \eta \, \rho \, (\nabla u)^2 & \nabla u < 0 \\ 0 & \nabla u \geq 0 \end{cases} \tag{16}$$

Here ρ denotes the fluid density, u is the particle velocity with its gradient $\nabla u.\eta$ is a geometry dependent factor defined as

$$\eta = \frac{\nabla u}{\nabla . u} \tag{17}$$

This factor reduces to unity for plane geometry. b in eq. (16) is an empirical constant determining the strength of the artificial viscosity q. The quadratic dependence on ∇u instead of linear dependence as observed in normal viscosity ensures that his term is small away from the shock. Also eq. (16) ensures that the artificial viscosity is absent during the expansion of the fluid.

The suitability and limitations of the von-Neumann procedure of artificial viscosity can be seen from Figure 1. In this figure we show the space profiles of the density and the pressure at various times of evolution for two test problems in plane geometry. The first test problem (Figure 1a and 1b) consists of a constant pressure applied at the right boundary of a 1.25×10^{-4} meter thick aluminium slab.

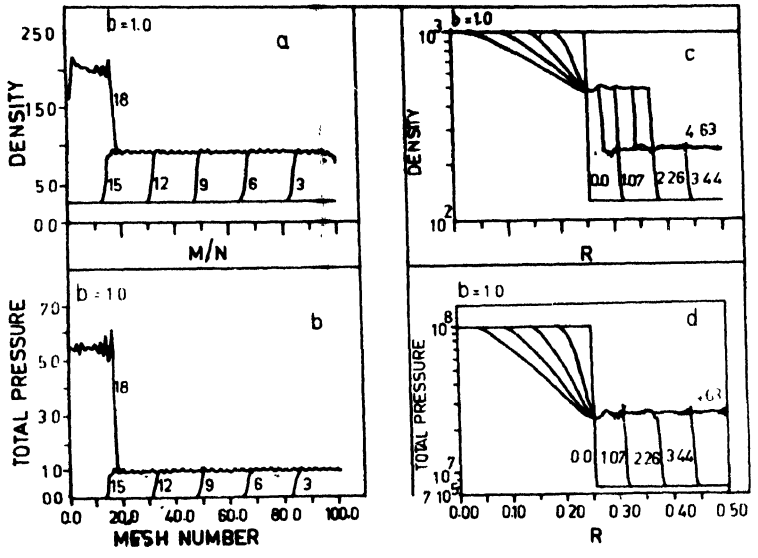

Figure 1. Density and pressure profile for constant pressure pulse and sod's problem using von - Neumann artificial viscosity.

This leads to a single shock wave moving towards the left, which is reflected at the fixed left boundary. The second test problem (Figure 1c and 1d) has its initial conditions given by

$$(\rho,u,p)^t = \begin{cases} (1.0,\ 0.0,\ 1.0)^t & R < R_0 \\ (0.125,\ 0.0,\ 0.1)^t & R > R_0. \end{cases} \tag{18}$$

This benchmark problem for shock wave calculations was proposed by Sod in 1978 [11]. Its exact solution consists of a shock wave propagating in the right direction ($R>R_0$), a rarefaction wave moving to the left ($R<R_0$) and a contact discontinuity separating the two. The results of the space profiles of density and pressure at various time steps are shown in Figures (1c) and (1d) respectively for this problem. The parameter $b = 1.0$ for the calculations presented in this figure. From this figure we observe that, although the artificial viscous pressure resolves the shock wave and the contact discontinuity well, it introduces some unphysical oscillations. The magnitude of these oscillations depend on the strength of artificial viscosity determined by the empirical parameter b. A low value for this parameter leads to high oscillations while a high value of it spreads the shocks over more meshes. Moreover, too high a value for artificial viscosity may falsify the results. For example, if the pressure pulse is caused by any oscillating particle or laser beam it may suppress some of the real oscillations associated with the beam. Also one can not be sure that at the point of interest

the artificial viscous pressure is zero because a small gradient in velocity will be amplified by the empirical factor b. In addition it is well known that the von-Neumann methods leads to high temperatures at contact discontinuity-shock interactions and at the point of shock reflection [12].

The need for a better technique to calculate variables at discontinuities is obvious from the above discussion. In recent years a class of new shock-capturing schemes have been developed which possess the above mentioned qualities. These schemes, usually referred to as "high resolution" schemes, have the following properties : (i) They are at least second order accurate on the smooth part of the flow; (ii) they sharply resolve discontinuities without generating spurious oscillations; (iii) they do not need artificial viscosity or other empirical prescription for shock capturing. The main building block of these schemes is an upwind scheme based on the exact [13] or an approximate [14] 'Riemann Solver'. A review of these schemes is given in Refs [15,16].

We describe one such scheme in the following subsection [17].

2.2. A high resolution shock capturing scheme :

The high resolution upwind schemes start with governing equations in conservation form *i.e.* a vector equation of the form

$$\frac{\partial W}{\partial t} \cdot \frac{\partial}{\partial m}\cdot[F(W)] = Q(W) \tag{19}$$

where W is the vector of conserved state variables, $F(W)$ is the vector of their fluxes and $Q(W)$ is the source vector. It is easy to recast eqs. (1–3) in the form of (19) with the following definitions of W, $F(W)$ and $Q(W)$

$$\begin{aligned} W &= (V, u, E)^t \\ F(W) &= (-r^\alpha u,\ r^\alpha p,\ r^\alpha up)^t \\ Q(W) &= (0,\ \alpha Vp/r,\ S)^t \end{aligned} \tag{20}$$

where E is the total specific energy defined as $U + 0.5\,u^2$. The method of operator splitting is used to solve (19), *i.e.* we decompose (19) into homogeneous system

$$\frac{dW}{dt} \frac{d}{dm}\cdot[F(W)] = 0 \tag{21}$$

and a system containing the sources

$$\frac{dW}{dt}\cdot = Q\ (W, r, t). \tag{22}$$

In each time step, these equations are solved sequentially. A second order accurate scheme is obtained by using a piecewise linear representation of the state variables in a grid zone through a monotonicity preserving interpolation of the form

$$W^n(m) = W_i^n + S_i^n(m - m_i) \tag{23}$$

where the subscript i denotes the value at the grid zone centre. The calculation of the vector of slopes S_n will be described later. We denote the right and left boundary values in each grid zone by $W_{i\pm}^n$. From eq. (23) we obtain these boundary values as

$$W_{i+}^n = W_i^n \pm \frac{\Delta m_i}{} S_i^n \tag{24}$$

These values are advanced to time $t^{n+1/2}$ using a Taylor expansion as

$$W_{i\pm}^{n+1/2} = W_{i\pm}^n - \frac{\Delta t}{2\Delta m_i}\left[F_{i+}^n - F_{i-}^n\right] \tag{25}$$

where

$$F_{i\pm}^n = F\left(W_{i\pm}^n\right). \tag{26}$$

This half time step establishes a second order accuracy in time. It only considers the development in time of the flow inside the grid zones. No fluxes between different cells are taken into account. Fluxes between the grid zones during the time step Δt can be calculated using the upwind scheme described in ref. [12] and one obtain the state variables at the next time step as

$$W_i^{n+1} = W_i^n - \frac{\Delta t}{\Delta m_i}\left[G\left(W_{i+}^{n+1/2}, W_{(i+1)-}^{n+1/2}\right) - G\left(W_{(i-1)+}^{n+1/2}, W_{i-}^{n+1/2}\right)\right] \tag{27}$$

where the numerical flux function G is as defined as

$$G\left(W_{i+}^{n+1/2}, W_{(i+1)-}^{n+1/2}\right) = \frac{1}{2}\left[F\left(W_{(i+)}^{n+1/2}\right) + F\left(W_{(i+1)-}^{n+1/2}\right)\right] - \frac{C_{i+1/2}^{n+1/2}}{2}\left[W_{(i+1)-}^{n+1/2} - W_{i+}^{n+1/2}\right] \tag{28}$$

where

$$C_{i+1/2}^{n+1/2} = \frac{\left(C_{i+}^{n+1/2} + C_{(i+1)-}^{n+1/2}\right)}{2} \tag{29}$$

C_i denotes the characteristic (or signal) velocities given by the theory of characteristics. For this we rewrite (19) in the quasi-linear form

$$\frac{\partial W}{\partial t} + A(W)\frac{\partial W}{\partial m} = Q(W) \tag{30}$$

where $A(W)$ denotes the Jacobain matrix $dF(W)/dW$. For $F(W)$ and W as defined by (20), we have

$$A(W) = r^{\alpha} \begin{bmatrix} 0 & -1 & 0 \\ \dfrac{\partial p}{\partial V} & -u\dfrac{\partial p}{\partial U} & \dfrac{\partial p}{\partial U} \\ u\dfrac{\partial p}{\partial V} & p - u^2\dfrac{\partial p}{\partial U} & u\dfrac{\partial p}{\partial U} \end{bmatrix} \tag{31}$$

whose eigenvalues—$C_L r^{\alpha}$, 0 and $C_L r^{\alpha}$ gives the required characteristic velocities. Here C_L denotes the Lagrangean sound speed defined as

$$C_L^2 = p\frac{\partial p}{\partial U} - \frac{\partial p}{\partial V} \tag{32}$$

and is related to the Eulerian sound speed C_E by C_E/V. This completes the numerical algorithm for one time step except for the definitions of the appropriate slopes in each grid zone. There are several ways to calculate the slopes. One can calculate them either in terms of the conservative variables V, u and E or in terms of the primitive variables ρ, u and p. The choice of conservative variables ensures the positivity of V and E. A simple form of slope calculation for each variable was proposed by van-Leer [18]

$$S = S(a,b) = \begin{cases} \dfrac{2ab}{(a+b)} & ab > 0 \\ 0 & ab \le 0 \end{cases} \tag{33}$$

where a,b stand for the right and left hand differences *e.g.* for the first variable

$$a = \frac{V_{i+1} - V_i}{m_{i+1} - m_i} \quad ; \quad b = \frac{V_i - V_{i-1}}{m_i - m_{i-1}}. \tag{34}$$

This form of slope calculation, though simple, sometimes leads to small oscillations. A better form of the slope calculation proposed by Roe [19,20] is

$$S = \frac{a}{|a|}\,\text{Max}\,\{|\text{Minmod}\,(a, S_k b)|\,,\ |\text{Minmod}\,(S_k a, b|\} \tag{35}$$

where the Minmod function is defined as

$$\text{Minmod}\,(a,b) = \begin{cases} a & |a| \le |b|\,, \quad ab > 0 \\ b & |a| > |b|\,, \quad ab > 0 \\ 0 & ab < 0 \end{cases} \tag{36}$$

S_k is a constant which takes a value between one and two. A value of 1.4 is recommended.

2.3. Solution for the source equation and discussions :

In each time step, the state variable vector W as obtained by solving the homogeneous eq.(21) has to be corrected for the sources by solving the source eq. (22). For a weak source one can use a fully explicit method where one writes

$$W_i^{n+1} = W_i^n + \Delta t\, Q\left(r_i,\, t_n,\, W_i^n\right). \tag{37}$$

Here W on the right hand side of this equation denotes the solution of a homogeneous equation as described in Section 2.1. In cases where the source term Q depends very strongly on the state vector W and time t one should use a fully implicit scheme

$$W_i^{n+1} = W_i^n + \Delta t\, Q(r_i, t_{n+1}, W_i^{n+1}). \tag{38}$$

or a combination of explicit and implicit schemes. Eq. (38) requires an iteration and hence more computational efforts. For a intermediate case one can use the predictor-corrector [21] method. In this method, we first obtain the 1st order predictor

$$\tilde{W}_i^{n+1} = W_i^n + \Delta t \cdot Q(r_i, t_n, W_i^n) \tag{39}$$

and than the 2nd order corrector

$$W_i^{n+1} = W_i^n + \frac{\Delta t}{2}\left[Q(r_i, t_n, W_i^n) + Q(r, t_{n+1}, \tilde{W}_i^{n+1})\right]. \tag{40}$$

To increase the accuracy, the second order corrector step should be repeated with the value of W_i^{n+1} on the left hand side of eq. (40) taken as $\tilde{W}_i^{n+1}$. Usually, one or two iterations are sufficient. For the purpose of demonstration of the numerical scheme three test problems are choosen for which analytical solutions are available. The first such test problem is the Sod's shock tube problem [11]. The initial conditions of this problem are

$$(\rho, u, p)^t = \begin{cases} (1.0,\ 0.0,\ 1.0)^t & R < R_0 \\ (0.125,\ 0.0,\ 0.1)^t & R > R_0 \end{cases} \tag{41}$$

The analytical solution consists of a shock wave, a contact discontinuity and a rarefaction wave. Our numerical solution using the 2nd order upwind scheme is compared with the analytical solution in Figure 2. The slope for the second order scheme was calculated using eq. (35) with the value of the constant $S_k = 1.4$. The comparisons in Figure 2 show that the corners of the analytical solution are rounded off in the numerical results. The constant state between the contact discontinuity and the shock wave are well reproduced by the numerical solution. The shock wave resolution is much sharper than that of the contact discontinuity. The second test problem we examine is the one proposed by Lax [22]. The initial conditions of this Riemann problem are

$$(\rho, u, p)^t = \begin{cases} (0.445,\ 0.698,\ 3.528)^t & R < 0.5 \\ (0.5,\ 0.0,\ 0.571)^t & R > 0.5 \end{cases} \tag{42}$$

Note that for this problem we have an initial jump in the particle velocity in addition to the jump in the density and the pressure which are also present in the Sod's problem discussed above. The results are compared with the analytical solution in Figure 3. Again, we observe that the shock wave is resolved very sharply but relatively large dissipation is introduced at the contact discontinuity. In the increasing order of complexity, the third test problem we consider here is one where a shock wave interacts with a contact discontinuity. Such a problem appears when the initial conditions are of the type

$$(\rho,u,p)^t = \begin{cases} (\rho_1,\ u_1,\ 10.0)^t & R<0.3 \\ (1.0,\ -1.0,\ 0.1)^t & 0.3<R<0.6 \\ (10.0,\ -1.0,\ 0.1)^t & R>0.6 \end{cases} \tag{43}$$

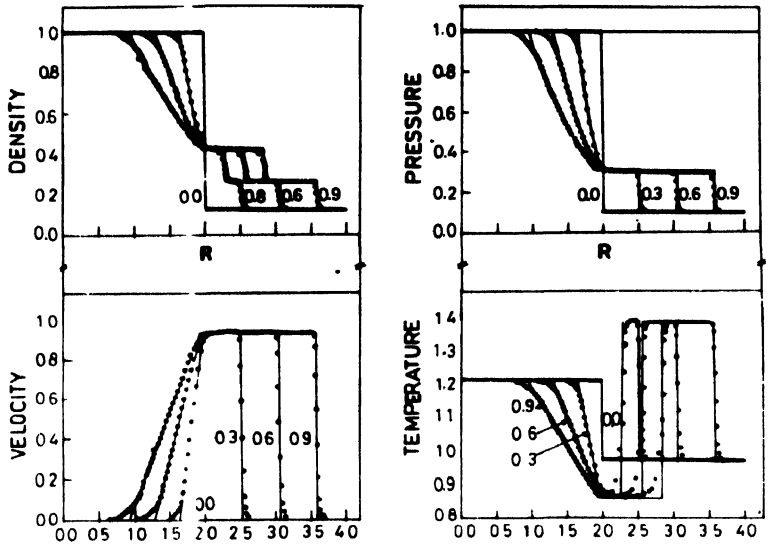

Figure 2. Space profiles for Sod's problem [11]. Solid lines represent analytical solutions while open circles give 2nd order upwind results.

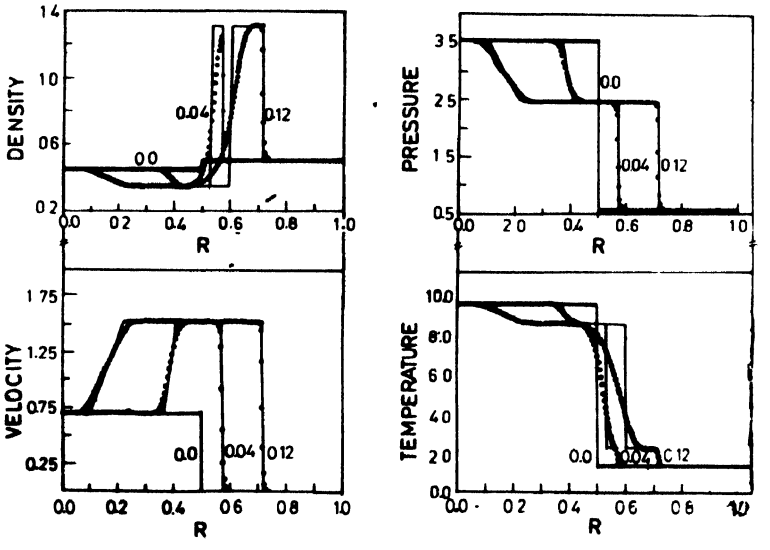

Figure 3. Space profiles for Lax's problem [22]. Solid lines represent analytical solutions while open circles give 2nd order upwind results.

Here we have a jump in density, velocity and pressure at $R = 0.3$ and a second jump in density at $R = 0.6$. The values of the constants p_1 and u_1 are so choosen that a shock wave is

generated at $R = 0.3$ moving towards right without the corresponding backward moving rarefaction wave. The values of p_1 and u_1 obtained using the well known Rankine-Hugniot relations are 1.856 and 5.67 respectively. The analytical solution of this problem consists of a shock wave initiated at $R = 0.3$ moving towards right and a contact discontinuity initiated at $R = 0.6$ moving towards left. These waves interact producing two shock waves and a contact discontinuity [23]. The analytical solutions are compared with the numerical results in Figure 4 for two time steps after the interaction of the shock wave and contact discontinuity.

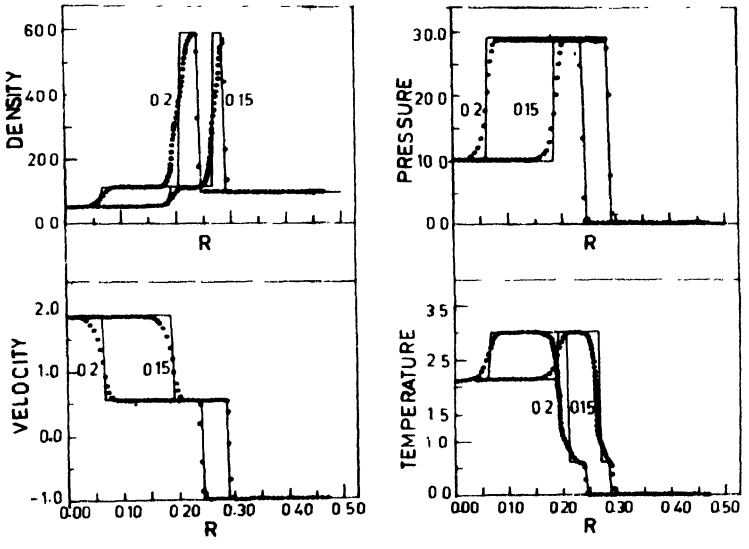

Figure 4. Space profiles for Munz's problem [23]. Solid lines represent analytical solutions while open circles give 2nd order upwind results.

3. Equation of state for ICF

The energy yield and hence the success of an ICF experiment largely depends on the level of compression one can achieve with a given driver. For a proper estimate of compression in an ICF numerical simulation, the need for an accurate EOS data is obvious. Most of the analytical or semi-analytical models on EOS can not cover a very wide range of densities and temperature. The density of the target may vary from as low as 10^{-3} times solid density ρ_0 in the corona region to 10^4 times ρ_0 in the central compressed region. Similarly, the temperature may vary from few Kelvines (cryogenic targets) to few KEV in the hot spark region. For a detailed study of EOS under these conditions the reader is referred to the recent book of Elizer, Ghatak and Hora [24] on this subject. From an user pint of view, the most accurate EOS data is available in tabular form (SESAME tables) developed in Los-Almos lab of USA [25]. These data do incorporate available experimental results and different theoretical models for different elements in different density and temperature ranges. However, for use in ICF applications these tables have two main problems. Firstly, these tables give total pressure and total internal energy while in ICF simulations one requires these quantities separately for

electrons and ions. Although, of late electron and ion EOS data for some selected elements have been incorporated in the SESAME tables, no claim is made about their accuracies. Therefore, one needs an additional prescription to separate out electron and ion contribution from total values given in the table. Secondly, from a practical point of view unless one has very efficient interpolation and more important the location search routines, the computational efforts involved may increase significantly. Thus it is necessary to develop some fast packages which evaluate EOS data on-line based on semi-empirical or theoretical models [26]. One such model which is observed to be efficient as well as fairly accurate will be described below. Any package on EOS should contain a model each for electron and ion and an appropriate prescription to estimate the average degree of ionization. We will describe these two features separately.

3.1. Average degree of ionization :

Average ionization of the plasma can be defined as

$$\bar{Z} = \Sigma_l C_l Z_l^* \tag{44}$$

where C_l is the fractional number density for the l–th element of the plasma and Z_l^* denotes the average state of ionization for the element. By definition

$$\sum C_l = 1$$

and the average ionization of the element Z_l^* is defined as

$$Z_l^* = \sum i\ C_l^i \tag{45}$$

where C_l^i denotes the fraction of atoms in the i-th state of ionization

An accurate estimate of $\bar{Z}$ in turn require an evaluation of C_l^i for each element.

The basic theory of ionization (especially useful in stellar interiors) provides the fraction C_l^i through Saha's equation [9] (subscript l is suppressed for convenience as future discussion restricts to one element case)

$$\frac{C_{i+1}.C_e}{C_i} = \frac{1}{\rho N} K_{i+1}(T) \tag{46}$$

where N is the total number density of the element ($C_i = N_i/N$) and C_e denotes the electron fraction. ρ is the plasma density. The function K is defined as

$$K_{i+1}(T) = A \frac{u_{i+1}}{u_i} T^{3/2} e^{-I_{i+1}/kT} \tag{47}$$

and constant A is given by

$$A = 2\left(2\pi m k/4^2\right)^{3/2} = 6.04 \times 10^{21}\ \text{eV}. \tag{48}$$

The electronic partition function u_i defined as

$$u_i = \sum_{R=0}^{\infty} g_k \, e^{-(\varepsilon_k - \varepsilon_0)/kT} \tag{49}$$

where g_k are the statistical weights for the level k and E_k are the energy levels for the i-ionized ion. Relation (46) represents a set of non-linear alzebric equations which can be solved iteratively to obtain C_i and hence $\bar{Z}$. However, an interpolation method [27] require much less computational efforts, less storage requirement and usually yields nearly the same results. This method proceeds as follows. If $Z^* \leq 1/2$, then it is assumed that only neutral and singly ionized atoms are present. In this case one obtains

$$Z^* = \frac{1}{2\rho N} \left\{ \sqrt{K_1^2 + 4K_1} - K_1 \right\}. \tag{50}$$

For the other extreme case when $Z^* \geq Z - 1/2$, one assumes the ions of charge Z and $Z-1$ are the only species present and this leads to

$$Z^* = \left(Z - 1 - \frac{K_2}{\rho N} \right) \sqrt{\left(Z - 1 - \frac{K_2}{\rho N} \right)^2 + \frac{4K_2}{\rho N}} \tag{51}$$

For any other intermediate value of Z^* one uses an interpolation formula of the type

$$Z^* = \frac{AT^{3/2}}{\rho N} \cdot \exp\left\{ - \frac{\bar{I}}{T} \right.$$

where the interpolated ionization potential $\bar{I}$ is defined as

$$\bar{I} = \left(n + 1/2 - Z^* \right) I_n + \left(Z^* + 1/2 - n \right) I_{n+1}$$

Saha equation in the present form has no provision to treat pressure ionization, a process arising at high densities and pressure where interaction among closely packed ions leads to the lowering of upper energy levels. More [27] proposed a simple procedure to incorporate pressure ionization in the Saha equation by a progressive reduction of equivalent statistical weight of excited levels, *i.e.* replacing the constants g_k in eq. (49) by a product $\pi_k g_k$ where the parameter π_k is 1 for low density (no pressure ionization) and goes smoothly to zero when reduced ionization energy of the ion approaches zero. Recently Busquet [28] pointed out that the above procedure of More spoils the principle of detailed balance since the ratio of upwards excitation rate W_{mn} to downwards de excitation rate W_{nm} has a value of π_m/π_n instead of unity as is required under the local thermodynamic equilibrium. He corrected the individual rate equations to include this parameter π_n so that the detailed balance is maintained. Alternatively many workers have proposed the use of average atom model to calculate Z^* [29]. However, all the above methods require storage of ionization potential and other atomic data for various ion species. An approach based on Thomas-Fermi model is free from such requirements. Thomas Fermi statistical model assumes that each nucleus is placed

at the centre of a sphere of radius R_0 given by $\left(\frac{3}{4\pi ni}\right)^{1/3}$ and within each sphere electrostatic potential is calculated by solving the poison equation. The potential is assumed zero at the outer surface of sphere and at the centre it approaches $\frac{Z_e}{r}$. For details see Ref. [24].

The ionization potential for any element of charge Z and average ionization Z^* is given by scaling

$$I(Z, Z^*) = Z^{4/3} I_0\left(\frac{Z^*}{Z}\right) \tag{52}$$

$$Z^* = Z.F\left(\frac{T}{Z^{4/3}}, \frac{\rho}{ZA}\right) \tag{53}$$

where $I_0(x)$ is found to be same for all the elements. Above potential is compared with exact HFS calculations for various elements and results are found in good agreement except for the absence of shell effects [30]. This form of scaling provides a universal scaling law for Z^* which does not need data storage for ionization potential. This scaling law can be written as where function F is defined as

$$F(x(T)) = \frac{x}{1 + x + \sqrt{1 + 2x}} \tag{54}$$

and

$$x = 14.3139 \left(\rho/ZA\right)^{0.6624} \qquad \text{for } T = 0$$

For $T \neq 0$, x is as defined below

$$x = 14.3139 \cdot Q^{0.6624}$$
$$Q = \left(R^C + Q_1^C\right)^{1/C}$$
$$C = C_1 T_F + C_2$$
$$T_F = T_0/(1 + T_0)$$
$$T_0 = T^{(eV)}/Z^{4/3}$$

$$R = \frac{\rho(g/c.c)}{ZA}$$
$$A = a_1 T_0^{a_2} + a_3 T_0^{a_4}$$
$$B = -\exp\left\{b_0 + b_1 T_F + b_2 T_F^7\right\}$$
$$Q_1 = AR^B$$

and constants $a_1 = 0.003323$, $b_0 = -1.7630$, $a_2 = 0.971832$, $b_1 = 1.43175$, $a_3 = 9.26148 \times 10^{-5}$, $b_2 = 0.315463$, $a_4 = 3.10165$, $C_1 = -0.36667$ and $C_2 = 0.983333$.

For an accurate evaluation of Z^* in the ICF condition, one can solve numerically the time dependent rate equation and such computer packages are available [31]. However, we have found that such a detailed calculations is not necessary and Thomas-Fermi model is advisable because of its efficiency and simplicity. Results presented in the next section use this model to calculate $\bar{Z}$.

3.2. Electron and ion EOS :

Ions being heavier pose no serious problems. A simple model for ion EOS gives reasonably good results. Even ideal gas EOS has been frequently used for ions without any serious problem. However, a better model based on the work of *R*. Cowan [32] is found quite suitable. The model gives explicit formulas for pressure and internal energy in three different regions of phase space. One region represent fluid state while the other two correspond to solid phase. The fluid region represents the temperature above the melting curve. The melting curve is obtained from the modified Lindemann Law [33]. The two solid state regions correspond to high and low temperatures and are represented by classical and Quantum Debye solid model. In both cases a Gruneisen parameter (with proper density-temperature scaling) gives pressure from the specific internal energy. Scaling formula is used for Debye temperature. The beauty of this model is that while it represents almost all elements it requires no constants. All material properties are represented only through atomic mass and atomic charge number. Further details of the model can be seen in Ref. [34]. EOS model for the electrons require complex treatment because of long electron De Broglie wavelength and hence classical models do not give good results. Furthermore, if high Z materials are present, as is usually the case, the large number of electrons in the plasma further demand an appropriate model for them. The earlier versions of ICF computer codes used Fermi-Dirac EOS [4,5] based on statistical mechanics of non-interacting particles which obey Pauli's exclusion principle. Here the pressure and energy are expanded interms of a degeneracy parameter.

$\xi = \frac{T}{TF}$; TF being the fermi temperature while T is the electron temperature. Different expansions are used in two different ranges of ξ. This model is found not to be sufficiently accurate, particularly when a high Z material is present in the target. The so called 'corrected Thomas-Fermi-Dirac' model for electrons [7] is found quite adequate for densities above the solid densities. It is based on the work of Bell [35] which incorporate Kirzhnits quantum and exchange corrections to Thomas-Fermi model. Further corrections are introduced by Tahir and Long [7] near the solid density. Various details of this model are beyond the preview of this paper and reader is referred to Ref. [7] for further details.

As an overall test, in Figure 5 we have compared the total pressure for 50–50 D–T mixture as obtained from the analytical models discussed in this section with the SESAME table values. Figure 6 shows similar comparisons for total internal energy. In both these figures the marker points represent the SESAME table values while solid line correspond to the model results. The average degree of ionization was calculated using the Thomas-Fermi scaling discussed in Section 3.1. Ideal gas EOS was used for ions while so called 'corrected Thomas-Fermi-Dirac' model with actual density was used for electrons. A wide variation of density from 10^{-3} to 10^{4} gms/cc was used while temperature varied from 10^{-3} eV to 10 KeV. From the figures we observe that a reasonably good agreement exists between SESAME table and the model except near the region of phase transition. A similar comparison is observed

even for heavier elements (results not presented in this paper because of space limitations). It is clear that further improvements are necessary for proper treatment of phase transitions. A detailed treatment of phase transition is incorporated in the Sandia Laboratory (USA) radiation hydrodynamic code package CHART-D [26]. However, for ICF related problems this transition phase is so short lived that simulation results may not be affected by these differences. However, in many of the experiments carried out in various laboratories engaged in ICF research where very high temperatures and compressions are not achieved, this discrepancy at phase transition may have to be looked into. At present at BARC, we are looking into various models to improve upon the representation of this phase transition. Point worth mentioning here is that the model for which results are presented in Figures 5 and 6 (solid lines) is computationally very efficient and the element is characterised only by its atomic mass and change number.

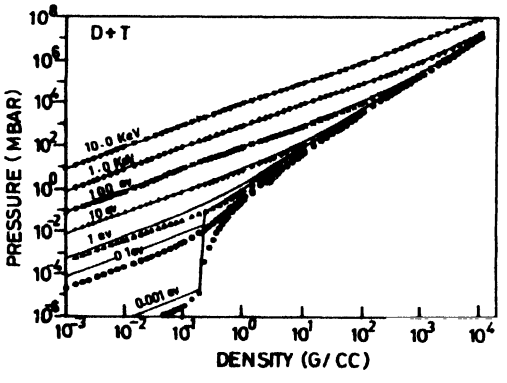

Figure 5. Pressure against density for D+T mixture. Points represent SESAME tables data while solid lines give calculated values.

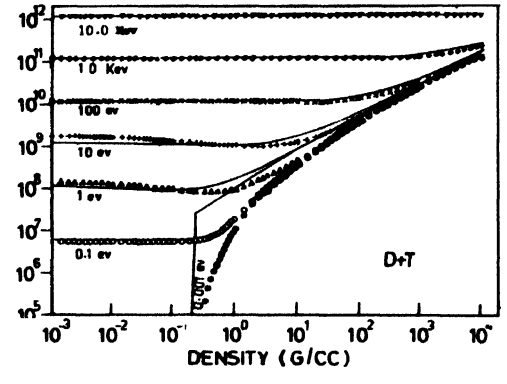

Figure 6. Specific internal energy against density for D+T mixture. Points represent SESAME tables data while solid lines give calculated values.

4. Beam energy deposition

As the energy deposition mechanism for Laser and ion beam are drastically different we discuss these two processes very briefly and separately in the following two subsections.

4.1. Laser energy deposition :

A prepulse (or tiny part of main Laser pulse) converts an ICF pellet to a partially ionized plasma with a density tail extending well beyond the core radius of the target. The absorption and scattering of laser light then predominantly occurs in this low density region. The energy is transported to the target surface by various heat conduction mechanisms. Predominant mode of laser absorption in the low density plasma is the classical inverse bremsstrahlung upto the critical density. At the critical density, the absorption and scattering is dominated by a number of non-linear process. A complete simulation of these mechanism is usually beyond the scope of ICF computer code. A empirical fit usually accounts for these non-linear processes. A commonly used prescription is to deposit a pre-prescribed fraction of laser light reaching at the critical density over a small zone (usually 2 to 3 space meshes) around the critical density and remaining light is reflected back to account for various scattering mechanisms. The back reflected light may again be absorbed by inverse bremsstrahlung while passing through low density plasma.

This simple prescription of laser light absorption require the prior knowledge of the space density profile of the corona region Many of the ICF codes ignore this initial phase and start the numerical simulation with the target in the form of a plasma. The energy consumed in this initial phase is small enough compared to overall energy balance so that no significant loss of accuracy is expected. However the effect of space profile of density on the absorption of laser energy require some study. For this purpose simulations are carried out for a 60 micro-gram 50–50 DT spherical pellet incident with CO_2 laser light of wavelength 1×10^{-5} meters. The radius of the pellet considered is 4.8×10^{-4} meters, and has a uniform density of 124.0 Kg/m^3. Laser pulse considered is of the shape

$$P(t) = P_0\left(1 - \frac{t}{\tau}\right)^{-5}. \tag{55}$$

This corresponds to the optimum pulse shape required for the generation of a converging sequence of shocks. P_0 is taken as 1.5×10^9 watts and pulse duration τ is 20.0 nano-seconds. The shape factor is taken as 2. Maximum laser power is restricted to 1.0×10^{16} watts and laser is switched off the moment it deposits a total of 4.0×10^3 Joules of energy to the plasma.

The plasma profile consists of a high density core of radius R_C surrounded by a low density tail of thickness R_T. Tail is considered to have a parabolic profile with density at tail beginning and end being 0.0248 and 0.00248 of the core density respectively [36]. Three cases are considered. For the first case the tail thickness is taken as zero and in this case all laser power is deposited at the outermost surface of the pellet. In case two $R_T = R_C$ and case three has thickness R_T twice the core radius.

In Figure 8 density and neutron production rates at the centre of sphere are plotted vs time. We note that the compressions achieved and the neutron yields are nearly the same in the three cases. However, there is a shift in the peak indicating that the hydrodynamics

motion is slightly sluggish in the presence of tail. In Figure 7 space profiles of density and ion and electron temperatures are shown at the time of maximum compressions. Space profiles are also seen to be similar in the three cases.

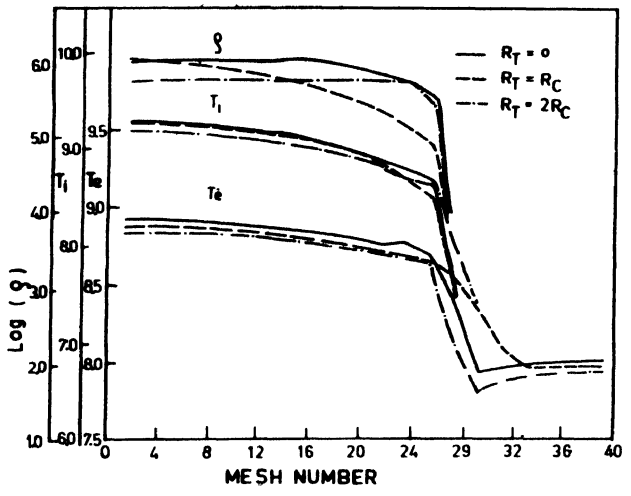

Figure 7. Space profiles for density and electron and ion temperatures for the three cases.

It is seen from the above study that if anomalous absorption is accounted for in a phenomenological manner then the presence of plasma tail does not affect the compressions, electrons and ion temperatures and hence the neutron and fusion yields except for a small delay in achieving the maximum yield.

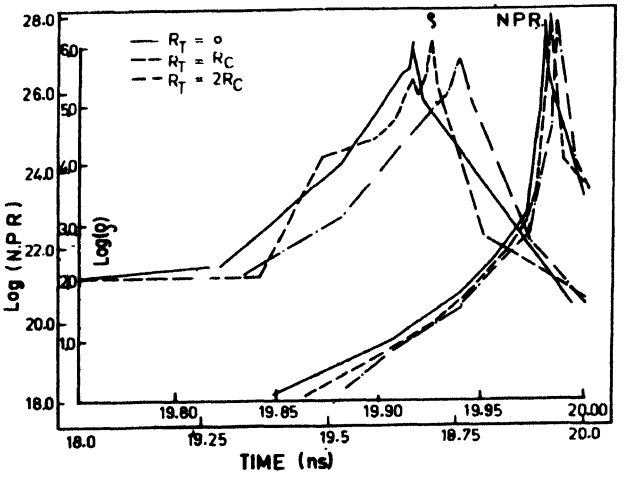

Figure 8. Time profiles for density and neutron production rate for the three cases.

4.2. Ion beam energy deposition :

A reasonably accurate estimate for the energy deposition profile $(1/\rho\ dE/dX)$ for the light and heavy ion beams in cold and hot plasmas is an essential feature for any ion beam

experiment simulation. The energy loss of ions in matter is primarilly due to the processes of ionization and excitation by coulomb forces. In hot plasma the collective plasma oscillations also contribute to the ion slowing down. It is anticipated that the ion beam energy coupling involves only linear processes as against the laser beam absorption which is dominated by non-linear effects. It is observed that a reasonable simplifying assumption is to calculate the slowing down of ion beam by bound electrons, free electrons and ions separately and then add them up. Binary collision theory within Debye sphere coupled with collective wave excitation outside the Debye sphere is usually sufficient to evaluate the contribution of beam slowing by free electrons and plasma ions. The slowing down model for bound electrons uses Bethe formula for high energy ions and Lindhard formula [37] for low energy ions. The Bethe equation accounts for both ionization and excitation of the atomic electrons and has the form [38].

$$\left(\frac{dE}{dX}\right)_{\text{BETHE}} = \frac{4\pi N_0 Z_{\text{eff}}^2 \rho e^4 Z}{m_e C^2 \beta^2 A}\left[\ln\frac{2m_e C^2\beta^2 r^2}{\langle I\rangle} - \beta^2 - \sum_i \frac{C_i'}{Z} - \frac{\delta}{2}\right] \quad (56)$$

where A and Z are the mass and charge atomic number of the stopping medium, Z_{eff} is the effective charge of the projectile ion, and all other symbols have their usual meanings. Note that the effective charge of projectile Z_{eff} depends on the energy of projectile and the state of plasma and hence it changes with time as the ion beam slows down in the plasma. The quantity $N_0\rho Z/A$ essentially gives the number density of bound electrons. The polarization effect correction term $\delta/2$ is usually small in the region of interest and the sum of shell correction effects $\sum_i (C_i/Z)$ is evaluated using the Mehlhorn's fitting formula. The Bethe's average ionization potential $\langle I\rangle$ is formally defined as

$$\ln\langle I\rangle = \frac{1}{2}\sum_n f_n \ln E_n \quad (57)$$

where E_n and f_n are the energies of possible electronic transitions and corresponding dipole oscillator strengths for the stopping medium. In practice, f_n and E_n are not known well enough and an accurate estimate of $\langle I\rangle$ is the main problem in estimation of ion energy deposition. A large amount of experimental data is available in the literature on the slowing down of proton beam in cold material and it has been fitted to the Bethe's formula by Anderson and Ziegler [39]. By such a fitting procedure, they have proposed a set of adjusted values $\langle I\rangle_{\text{Adj}}$ for the average ionization potential for all elements from $Z = 2$ to $Z = 93$ for cold materials. However, no such experimental data is available at temperature of interest in ICF conditions so as to obtain a similar set of adjusted values of $\langle I\rangle$ at high temperature. Mehlhorn proposed an interpolation of the form

$$\langle I(Z,q)\rangle = \left(\frac{Z}{Z-q}\right)^2 \langle I(Z-q,0)\rangle \quad (58)$$

where $\langle I(Z-q,0)\rangle$ denotes the average ionization potential for the cold material and q denotes the ionicity of the stopping medium. $q = 0$ for the neutral and $q = Z$ for the fully ionised material. In the latter case, the term mean ionization potential does not make any sense and hence the maximum value of q is restricted to $Z-1$. The above expression is by definition accurate for $q = 0$ (neutral atom) and for $q = Z-1$ (hydrogenic atom). However, it was soon realised that this interpolation can give qualitative results but for reasonably accurate quantitative estimates of ion beam slowing down by bound electrons, a more accurate value of $<I>$ is essential. For a few selected elements $<I>$ have been evaluated from the first principles using time consuming atomic calculations, *e.g.* McGuire *et al* [40] have evaluated $<I>$ for aluminium using such an approach. However, one needs an efficient formulation to evaluate $<I>$ on line with an ICF computer code. Such a formulation was recently developed by Goel and Gupta [41] based on screened hydrogenic atom (SHA) model of More [42]. In Figure 9 we compare the stoping power of uniformly ionised plasma as calculated by the procedure described above with $<I>$ calculated from SHA model with those obtained from the first principle generalised oscillator strength calculation of McGuire [43]. Various curves in the figure denote the degree of ionization. In general a good agreement is observed for low values of ionicity and fairly good for highly ionized plasma.

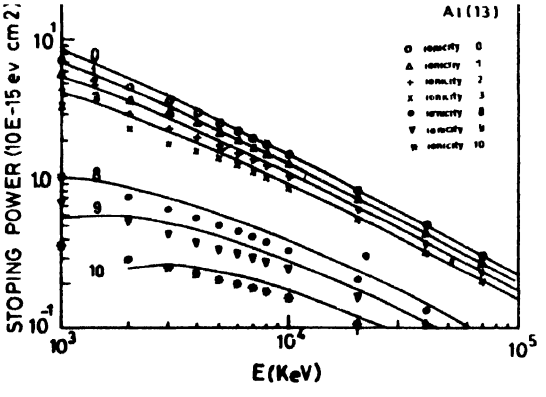

Figure 9. Stoping power of proton beam in aluminium. Solid lines represent calculated values while points give McGuire values

5. Concluding remarks

In this paper, we have described three main aspects of our one dimensional Lagrangean geometry ICF code. The von-Neumann method of artificial viscous pressure to treat shock waves is observed to give higher temperatures at shock reflection and at shock wave interactions. Instead, the high resolution upwind schemes are recommended. Except for the region of phase transition, our semi-empirical model for EOS is found satisfactory. Some results for the laser and ion beam energy deposition are also presented in this paper.

Acknowledgments

Part of the work reported in this paper was carried out at Institut für Neutronenphysik und Reactortechnik, Kernforschungszentrum, Fed. Rep. Germany during one of the authors (NKG) stay there.

Note added in the proof

This review is certainly not exhaustive on the subject as it covers only three of the many aspects of I C F numerical simulation. In particular, our efforts on the subject of radiation transport and computation of multi-group radiation opacities are not included in this paper.

References

[1] J J Duderstat and G A Morse 1982 *Inertial Confinement Fusion* (New York John Willey)

[2] F Winterberg 1980 *Z. Physik* **A296** 3

[3] J H Nuckolls, L Wood, A Thiessen and G B Zimmerman 1972 *Nature* **239** 139

[4] J P Christiansen, D E T F Ashby and K V Roberts 1974 *Comput. Phys. Commun.* **7** 271

[5] N K Gupta and S V Lawande 1983 *Numerical Simulation of Laser Driven Fusion* **BARC/I-776**

[6] G B Zimmerman 1973 *Numerical Simulation of High Density Approach to Laser Fusion* **UCRL-74811**

[7] N A Tahir and K A Long 1983 *MEDUSA-KA A One Dimensional Computer Code for Inertial Confinement Fusion Target Design* **KfK-3454**

[8] S L Thompson and H S Lanson 1974 *Improvement in the Chart Radiation Hydrodynamic Code II A Revised Program* **SC-RR-710713**

[9] Ya B Zeldovich and Yu P Raizer 1968 *Elements of Gas Dynamics and Classical Theory of Shock Waves* (New York Academic)

[10] R D Richtmyer and K W Morton 1976 *Difference Methods for Initial Value Problems* 2nd eds (New York John-Wiley)

[11] G A Q Sod 1978 *J. Comput. Phys.* **27** 1

[12] N K Gupta, C D Munz and B Goel 1990 *High Resolution Shock Capturing Scheme for Numerical Simulation of Plasma-Shock Interaction* **KfK-4696**

[13] S K Godunov 1959 *Mat. Sbornik* **U7** 271

[14] B Einfeldt 1988 *SIAM J. Numer. Anal.* **25** 294

[15] A Harten 1984 *SIAM J. Numer. Anal.* **21** 1

[16] A Harten, P D Lax and B Van Leer 1983 *SIAM Rev.* **25** 35

[17] N K Gupta, C D Munz and B Goel 1990 *Laser and Particle Beams* **8** 807

[18] B Van Leer 1979 *J. Comput. Phys.* **32** 101

[19] P L. Roe 1981 *J. Comput. Phys.* **43** 357

[20] P K Sweby 1984 *SIAM J. Numer. Anal.* **22** 995

[21] J Stoer and Bulirsch 1978 *Einfuhrung in die Numerische Mathematik* (Berlin : Springer-Verlag)

[22] P D Lax 1954 *Comm. Pure Appl. Math.* **7** 159

[23] C D Munz 1988 *J. Comput. Phys.* **77** 18

[24] S Eliezer, A Ghatak and H Hora 1986 *An Introduction to Equation of State, Theory and Applications* (Cambridge : Cambridge University Press)

[25] B I Bennet, J D Johnson, G I Kerley and G T Rood 1978 *Recent Development in the Sesame Equation of State Library* **LA-7130**

[26] S L Thompson and H S Lauson 1972 *Improvement in Chart D Radiation Hydrodynamic Code III : Revised Analytic Equation of State*

[27] R M More 1982 *J. Quant. Spectrosc. Radiat. Trans.* **27** 345

[28] M Busquet 1990 *J. Quant. Spectrosc. Radiat. Trans* **43** 91

[29] G B Zimmerman and R M More 1980 *J. Quant. Spectrosc. Radiat. Trans.* **23** 517

[30] R M More 1985 *Adv. Atom. Molec. Phys.* **21** 305

[31] J Magil 1978 *TRIP-A Time Dependent Recombination and Ionization Package, Comp. Phys. Comm* **16** 129

[32] C W Cranfill and R More 1978 *Ioneos : A Fast, Analytic Ion Equation of State Routine* **LA-73IM-MS**

[33] R Grover 1975 *Generalized Lindemann Law for Simple Solids* **UCRL-76544**

[34] R M More, K H Warren, D A Young and G S Zimmerman 1988 *Phys. Fluids.* **31** 3059

[35] A R Bell 1981 *New Equation of State for MEDUSA Rutherford Lab. Report* **RI-80-091**

[36] E B Goldman 1973 *Plasma Phys.* **15** 289

[37] J Lindhard and M Scharff 1961 *Phys Rev.* **124** 128

[38] T A Mehlhorn 1981 *J. Appl. Phys.* **52** 6522

[39] H H Anderson and J F Ziegler 1977 *Hydrogen Stoping Power and Ranges in All Elements* (New York Pergamon)

[40] E J McGuire, J M Peek and Pitchford 1982 *Phys* Rev. **A26** 1318

[41] B Goel and N K Gupta 1989 *Proc. 5th Inte. Conf. Emerging Nuclear Energy Systems, Karlsruhe 3–6 July* p 153

[42] J M More 1982 *J. Quant. Spectrosc. Radiat. Trans.* 345

[43] E J McGuire 1982 *Phys. Rev.* **A26** 1871